# Analyst

## Accepted Manuscript

This article can be cited before page numbers have been issued, to do this please use: Y. Yu, Q. Zhang, C. Chang, Y. Liu, Z. Yang, Y. Guo, Y. Wang, D. Galanakis, K. Levon and M. H. Rafailovich, *Analyst*, 2016, DOI: 10.1039/C6AN01157H.

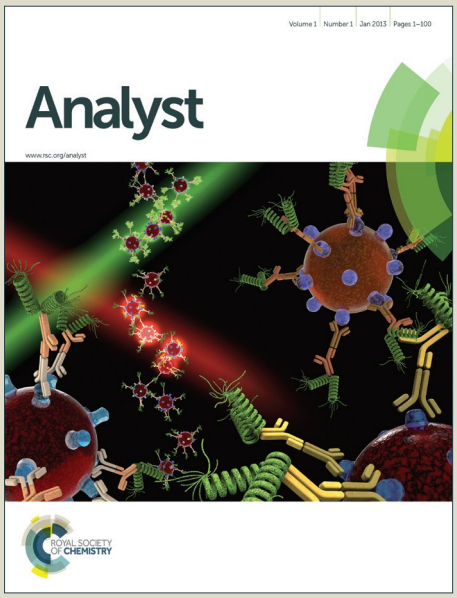




ROYAL SOCIETY OF CHEMISTRY

www.rsc.org/analyst

View Article Online
DOI: 10.1039/C6AN01157H

# Design of molecular imprinting biosensor with multi-scale roughness for the detection across a broad spectrum of biomolecules

Yingjie Yu[a, *], Qi Zhang[b], Chung-Chueh Chang[c], Ying Liu[c], Zhenhua Yang[a], Yichen Guo[a], Yantian Wang[a], Dennis K. Galanakis[d], Kalle Levon[b], Miriam Rafailovich[a,*]

[a]*Department of Materials Science and Engineering, Stony Brook University, Stony Brook, NY, 11794. USA.*
[b]*Department of Chemical and Biomolecular Engineering, New York University Tandon School of Engineering, Brooklyn, NY, 11201,USA.*
[c]*ThINC Facility, Advanced Energy Center, Stony Brook, NY 11794. USA.*
[d]*Department of Medicine, Stony Brook University School of Medicine, Stony Brook, NY, 11794,USA.*

*Corresponding Author:
Tel: +1 631-880-9687
Email address: yuyingjie312@gmail.com (Y.Yingjie)
Tel: +1 516-458-9011
Email address: miriam.rafailovich@stonybrook.edu (R.Miriam).

**Keywords:** Multi-scale roughness, self-assemble monolayer (SAM), molecular imprinting (MI), open circuit potential (OCP)

**Abstract**

Molecular imprinting technique has tremendous applications in artificial enzymes, bioseparation, and sensor devices. In this study, a novel molecular imprinting (MI) biosensor platform was developed for the detection of a broad range of biomolecules with different sizes. Previously this method has been applied to 2D molecular imprinting, where the height of the self-assembled monolayer (SAM) at around 2 nm limited the maximum dimensions of the molecule that can be imprinted to create template-shaped cavities. In order to match the size of the imprinted molecules with the height of the SAM, we propose a model for 3D molecular imprinting, where the analyte is sequestered within a niche created by the surface roughness. The SAM is assembled on the walls of the niche, forming a 3D pattern of the analyte uniquely molded to its contour. The surfaces with multi-scale roughness was prepared by evaporation of gold onto electropolished (smooth) and unpolished (rough) Si wafers, where the native roughness was found to have a normal distribution centered around 5 and 90 nm respectively. Our studies using molecules ranging in a nanometer scale, from proteins of a few nanometers to bacteria of hundreds of nanometers, showed that when the size of analyte matched the roughness range of the gold surface, the molecular imprinting process was optimized for the best biosensing performance. After optimization, the MI biosensor platform enabled the identification and quantification of a broad set of biomolecules with great discrimination abilities. Hemoglobin under different pH value could be well distinguished via MI biosensor. Several mutated fibrinogen molecules can also be well differentiated through the test.

View Article Online
DOI: 10.1039/C6AN01157H



## Introduction

Electrochemical biosensing enables highly sensitive detection of analytes and transmission of data wirelessly to remote areas.[1-12] They have the potential of being integrated into smart responsive biomedical systems, such as sequencing devices[13], triggered drug delivery platforms[14-18]and rapid pathogen sensors that report to medical personnel. Compared to the traditional immunohistochemistry, electrochemical sensors provide results quickly, are inexpensive and portable[4, 5, 19]. In our previous study, electrochemical detection was presented as an ideal alternative to conventional ELISA for protein biomarker quantification[20]. Moreover, DNA chips producing electrical signal have long been proposed[21, 22]. Recently, Miao et al pioneered ultrasensitive biosensors for microRNA as a crucial biomarker for diagnosis and prognosis of cancers[23-25]. In addition to clinical uses, electrochemical sensors have been widely applied in environmental monitoring. Multiple sensing approaches have been devised by Chen et al to quantify Escherichia coli and Staphylococcus aureus in drinking water[26, 27].

Herein, we present a surface molecular imprinting (MI) technology that provides a real-time and label-free sensing interface to be integrated into the devices.[28-38] Unlike the traditional molecular imprinting polymers, the process of surface molecular imprinting is very gentle. No harsh chemical reaction process is required, which greatly improves the applicability of biosensor in protein. Although there are enormous amount of research on biosensor in the past two decades, most of them are only capable of detecting certain analyte based on their special property or relationship between analyte and the interface.[19, 26, 39-42]Designing a biosensor platform, applicable to a broad set of the biomolecules, can greatly improve the detection efficiency. Hence, molecular imprinting, based on the classic “lock and key” model, turns out to be a universal detection platform for application on various analyte[43-47]. With the unique structure and conformation of the biomolecules, different analytes, such as protein, antigen, virus, can be easily differentiated by MI biosensor. Atar et al combined molecular imprinting technical with surface plasma resonance to design nanosensor for several analytes, achieved great sensitivity for detection of amikacin and triclosan.[48, 49] Therefore, molecular imprinting platform could be used as a great biosensing platform for tracing amount of analyte.

The technique of surface molecular imprinting was first used octadecyltrichlorosilane (OTS) self assembled monolayers for imprinting amino acids on ITO electrodes[50]. This technique could be so sensitive that it was able to not only differentiate between different molecules, but also determine their chirality. The drawbacks though were the fact that OTS is hydrophobic and the method is limited to analytes soluble in non-polar solvents. Furthermore, they showed that the technique was only able to sense molecules whose dimensions were similar to the OTS layer thickness, or 2 nm. Later, Wang et al showed that larger bio macromolecules, could also be detected if the imprinting SAM was made with hydrophilic moieties, such as -OH terminated thiols[46, 51], which provides hydrogen bonds between the hydrophilic groups on protein surface and the hydroxyl groups. In their study, entire proteins were detected rather than single small amino acids, which was inconsistent with the early predictions which postulated that the technique was limited to analytes not significantly larger than the thiol monolayer thickness[50]. We then proposed that the surface

View Article Online
DOI: 10.1039/C6AN01157H



roughness of the imprinting electrode could also be a contributing factor in the molecular imprinting process. Therefore, the dimension that limits the size of the imprinted analyte was not simply the SAM layer thickness, but also the size of the analyte relative to the surface roughness. Hence, when the imprinting was done with OTS on a ITO glass whose surface roughness was 0.6 nm, the SAM layer thickness, of approximately 2 nm was the larger and hence the limiting dimension[50, 52]. When imprinting was done with OH-terminated thiols assembled on gold-coated Si electrodes, the RMS roughness of the gold, much higher than the SAM layer, and dimensional limit of the analytes which could be detected was increased.

We therefore propose a 3D molecular imprinting model where the efficiency and sensitivity of the potentiometric biosensor could be enhanced even more if the surface roughness was tailored to match the size of the analyte molecule. In this model the surface morphology formed a niche which surrounded the analyte and the SAM formed a precise coating surrounding the analyte in three dimensions. In this manner one would be able to significantly increase the range of detectable analytes, and the versatility of the technique. In our previous study, a CEA biosensor based on MI was successfully designed, and applied to the detection in patient cyst fluid[53]. The result obtained from MI biosensor is comparable to the result detected through ELISA, but required much less time. In this contribution, we designed the MI biosensor on multi-scale roughness surface, by matching the analyte size to the proper gold surface. This MI biosensor can be extend the to the detection of a much wider spectrum of biomolecules with different sizes ranging from a few nanometer proteins to hundreds of nanometer virus.

## Materials and Method

### 2.1. Materials

The analytes used for molecular imprinting are listed in Table 1. Carcinoembryonic antigen (CEA) from human, myoglobin (Mb) from equine skeletal muscle (Mw = 17.6 K Da), hemoglobin (Hb) from bovine blood (Mw = 64.5K Da), and routine chemical reagents were from Sigma–Aldrich. Human fibrinogen was isolated [54] from pooled volunteer plasma under institutional IRB-approved human subject research protocol.[55, 56] Imprinting was performed using 11-mercapto-1-undecanol (SH-$(CH_2)_{11}$-OH; 97%, Aldrich), and dimethyl sulfoxide (DMSO) from Sigma Aldrich.

### 2.2 Gold substrate physical vapor deposition

Gold/chromium substrates were prepared by the physical vapor deposition of gold onto silicon wafers in a high-vacuum evaporator at $10^{-7}$ Torr. Silicon wafers substrates were preheated to 325 °C for 2 hours by a radiation heater before deposition. Evaporation rates were 0.1- 0.3 nm/s, and the final thickness of the gold films was around 100 nm.

### 2.3 MI biosensor fabrication

View Article Online
DOI: 10.1039/C6AN01157H



In order to fabricate the gold surface with different roughness, first a 10 nm layer of chromium was deposited onto the Si substrate to facilitate adhesion, followed by a 100 nm coating of gold. The coatings were deposited on either the smooth or the rough side of the silicon substrate using electron beam evaporation in a vacuum of $10^{-7}$ Torr in the Cornell NanoScale Facility (CNF). The gold-coated substrate (1.5 cm × 2 cm) was rinsed with ethanol and dried under nitrogen gas. The gold electrode was then covered in Teflon tape leaving an open active circular area of 1.2 cm in diameter for imprinting. In this manner the responses from different sensor electrodes could be quantitatively compared.

To make the SAM on gold surface, different ratios of thiol/DMSO and analyte/de-ionized water were prepared. Thiol and analyte blend solutions were made as follows: the templating analyte was dissolved in de-ionized water and the alkanethiols, were dissolved in DMSO. The two solutions were mixed (19/1 [v/v], respectively) to a 100 μM final thiol concentration. The final concentration of the imprinted analytes, such as Hb, Mb, CEA, and Fb, were 0.465 μM, 1.7 μM, 0.0075 nM and 0.059 μM, respectively. For poliovirus and adenovirus were $1.5 \times 10^8$ and $5.0 \times 10^7$, respectively.

The prepared gold-coated electrode was then immersed into the analyte/thiol imprinting solution at room temperature for 2.5 hours and soaked into 1 M NaCl solution for 1 hour to remove the templating molecules.

2.4 Electrochemical measurements

The analytes were assayed in a beaker containing 10 mL of 1x PBS detection medium continuously stirred with a magnetic stirrer. A potentiometer (Lawson Laboratories, Model E13) was utilized to monitor the potential change of the MI biosensor. An Ag/AgCl electrode was connected to reference channel and the imprinted gold chip was connected to working electrode channel. A fixed amount of the analyte solution was pipetted drop-wise into the detection medium, and the open circuit potential (OCP) was monitored real-time using L-EMF DAQ software.

Electrochemical impedance spectroscopy (EIS) measurements were performed using a CHI 660d electrochemical workstation (CH Instruments) with a three electrodes system. It consists of a gold chip electrode, with or without molecular imprinting, as the working electrode, a platinum wire as the counter electrode and an Ag/AgCl electrode (BASi) as the reference electrode.

## Results

### 3.1 Surface characterization

(a) Surface topography characterization was operated using AFM. In Figure 1 (A), (B) we show a 3D view of the AFM topographical scans of the smooth and rough gold coated silicon substrates, together with typical cross sectional scans showing how the surface morphology was analyzed. The distribution of both horizontal and vertical length scales for the roughness on the smooth and rough gold surfaces are plotted in Figure 1(C) and (D), respectively. Two distinct Gaussian curves are obtained. On the smooth gold surface the distribution is narrow, with the horizontal mean roughness being approximately twice as large as the

View Article Online
DOI: 10.1039/C6AN01157H



vertical mean roughness of 3.4 (±0.5) nm. While on the rough gold surface, the distribution is much broader with the mean horizontal spacing being approximately five time larger than the mean vertical roughness of 17 ( ± 5.3 ) nm. Therefore, the gold surface with multi-scale roughness was conveniently prepared by gold PVD on smooth and rough side of silicon substrate.

(b) Surface wettability was characterized using contact angle goniometry. In Figure 1 (E) we show the water contact angle obtained on the two bare gold surfaces and the surfaces after they are covered with a SAM without imprinted analytes. Although the surface physical roughness are different on the two surfaces.

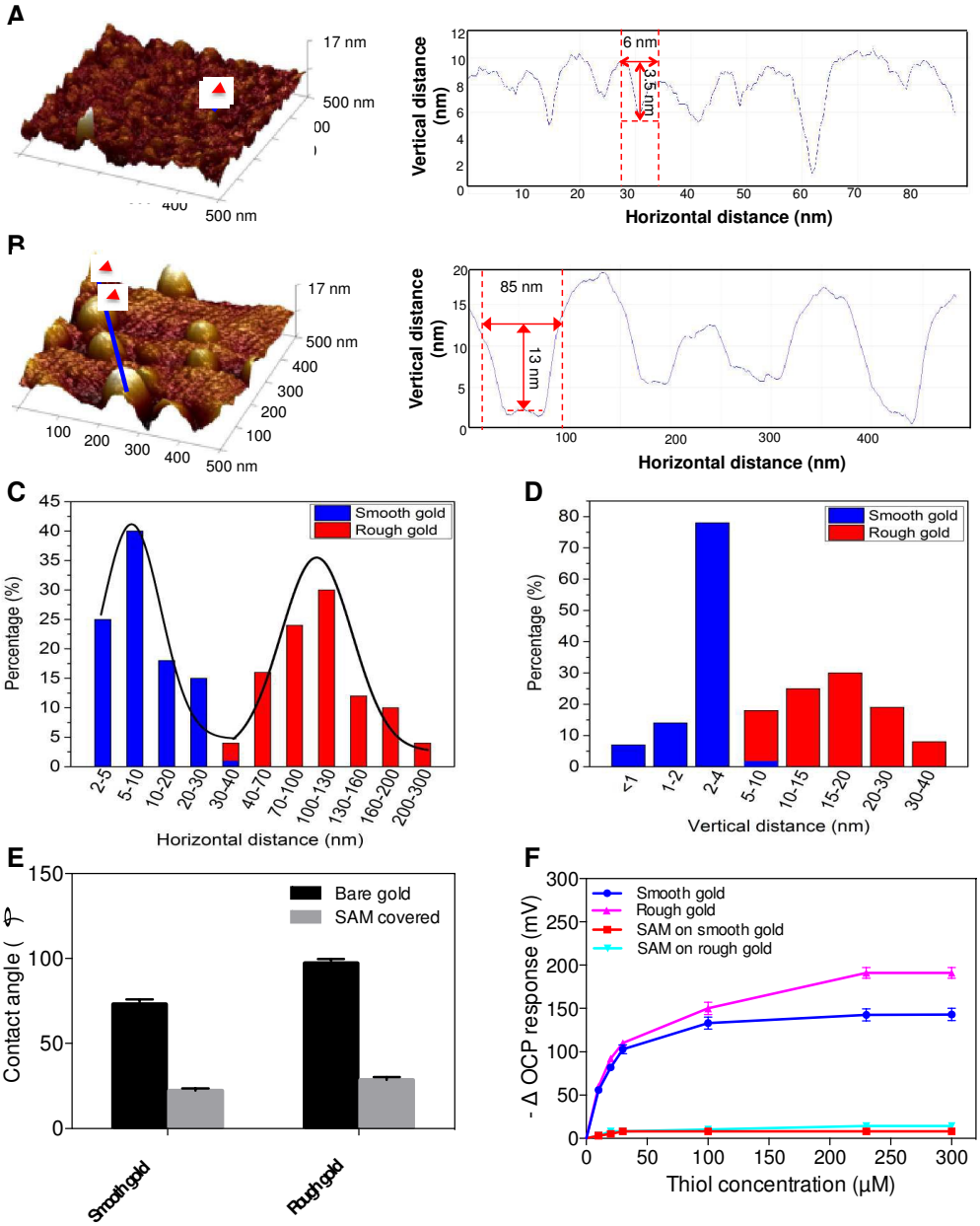


**Fig.1. Surface characterization of multi-scale roughness gold surfaces.** AFM topographical scan and the associated cross sectional analysis for A) smooth and B) rough gold surfaces. Further description of the surfaces by histogram of C) horizontal and D) vertical surface roughness for smooth and rough gold

View Article Online
DOI: 10.1039/C6AN01157H

surfaces is shown. Comparison between smooth and rough surfaces before (bare gold) and after (SAM covered) SAM formation characterized by E) contact angle and F) potentiometric titration with thiol solution. Similar chemical property was found on both smooth and rough gold surfaces after SAM formation, despite of the large physical roughness difference between them.

their contact angles decrease to the same value of 23 ± 1.6 degrees, confirming that they are both fully coated with identical surface chemical properties. Hence the two surfaces differ mostly in degree of topographical roughness, while their surface properties are very similar.

### 3.2 Electrochemical characterization

The area occupied by the imprinting molecules can be determined by titrating the amount of thiols on gold surface. It is well established that thiol molecules are adsorbed to the gold surface through strong sulfur-Au bond to form SAM via the electron transfer reaction, [31, 57]

***Equation 1***: $R\text{-}S\text{-}H + Au \rightarrow R\text{-}S\text{-}Au + e^- + H^+$

Therefore the thiol-Au adsorption process could be studied by observing the OCP change generated from transfer of the free electron to the gold conducting layer. In order to determine the area fraction on bare gold surface, the gold electrode was inserted into the detection solution, and a titration solution of 0.4 mg/ml thiols was added in the analysis chamber, while the OCP change was generated by the free electron released in the reaction was recorded. The data for the OCP on the bare gold and the fully covered surfaces are shown in Figure 1F.

In order to determine the OCP generated when the gold surface is fully covered by thiol molecules, the bare gold electrode was inserted into the detection solution (1x PBS buffer) and thiols were added till a plateau region in the OCP was reached indicating the surface was fully covered. The response curves are shown in Figure 1F, where we see that on the smooth surface a plateau value of 120 mV was obtained when a total of 100 μM of thiols were added. Since no further increase in the OCP response occurred when additional thiols were added, the value at the onset was taken to correspond to the OCP generated as the surface coverage was completed. This was further confirmed using electrochemical impedance spectroscopy (EIS), which suggested the maximum conductivity for the bare gold surface and the minimum for the gold surface fully coated by thiol (Figure S1 in supplementary materials). Since the area exposed to the thiol solution is the same in all experiments, we can conclude that the rough side of the Si wafer exposes approximately 100 percent gold additional surface area. This additional area is required for the detection of the larger analytes and is responsible for the larger OCP responses observed.

### 3.3 Analyte introduction

View Article Online
DOI: 10.1039/C6AN01157H



In order to probe the degree to which surface roughness and analyte size resonate to maximize the open circuit potentiometric signal, both smooth and rough gold electrodes were imprinted with analytes with different dimensions. The relative sizes of the analytes used are compared to each other in Figure 2A, sorted by their vertical dimension, which ranges from 5 nm to more than 2 μm. In order to span this large range, more than 10 types of analytes were used that cover a broad gamut of biological molecules ranging from proteins, antigen, viruses, to bacteria. In Table 1, the sizes and the molecular weights of all the analytes we used in this study are summarized [58-64].

Table 1 Summary of the sizes and molecular weights of analytes in this study

| Analyte | $M_w(\times 10^3)$ | Dimension (nm) | Shape | Reference |
|---|---|---|---|---|
| Mb | 17.6 | 3.5×2×4.5 | Rectangle | 40 |
| Hb | 64.5 | 5×5×5 | Rectangle | 41 |
| CEA | 200 | 8×28† | Cylinder | 42 |
| Fb | 340 | 9×6×47 | Rectangle | 40 |
| Poliovirus | N/A | 20 ‡ | Sphere | 43 |
| Adenovirus | N/A | 90 ‡ | Sphere | 44 |
| S. Aureus | N/A | 600 ‡ | Sphere | 45 |
| E.Coli | N/A | 500×2000† | Cylinder | 46 |

† The shape of molecule is cylinder, the first number represents the radius of undersurface, and the second number represents the height of cylinder.

‡ The shape of the molecules is sphere; the number represents the diameter of the sphere.

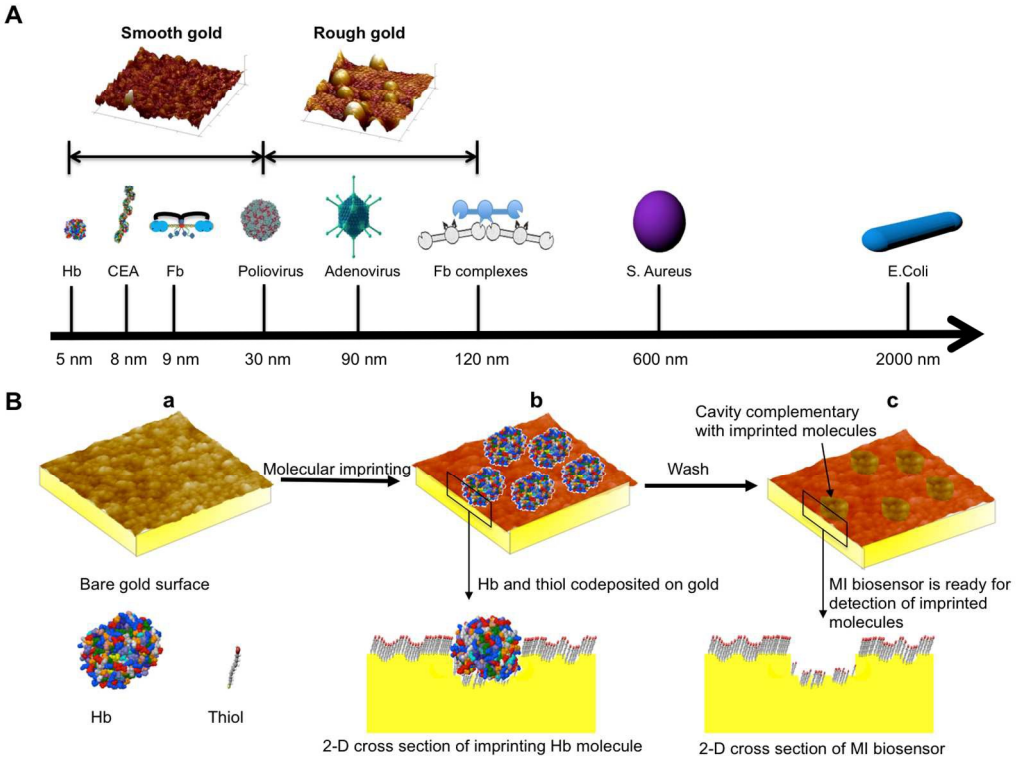

View Article Online
DOI: 10.1039/C6AN01157H



**Fig.2. A summary of analytes and fabrication process of the MI biosensor.** (A) Size distribution of the possible analytes in this study, including protein, antigen, virus and bacteria in different sizes, as plotted on a nanometer scale chart. (B) Schematic illustration and cross-sectional of the 3D MI biosensor fabrication process. The red-color layer represents SAM coverage.

The basic elements of the MI process are illustrated in Fig 2B. Analyte and thiol are co-deposited on the gold-coated Si electrodes, where the analyte sits somewhere in the surface niche created by the gold and is then enveloped by the self assembled OH-thiol monolayer. The analyte is then removed by being soaked in 1M NaCl solution and leaving behind a template of itself, as shown. It should be noted that the cartoon in Figure 2 (B) is a two dimensional cross-section of the imprinted cavity. In reality, the imprinted pattern is three dimensional, where the thiolated layer fills all space between the analyte and the surfaces of the niche.

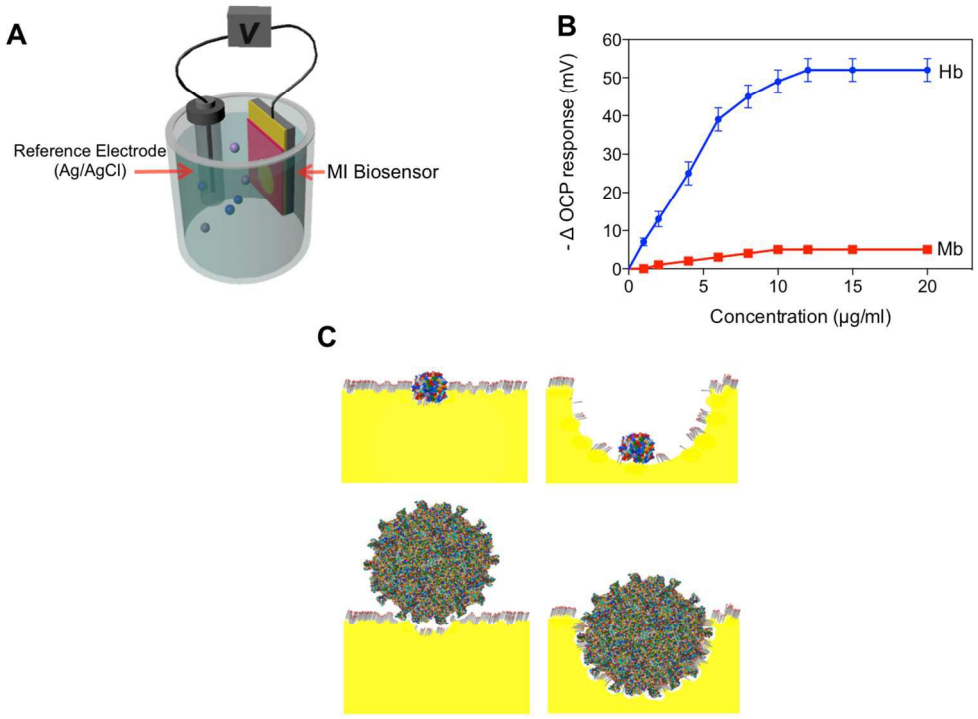


**Fig.3. OCP detection method on multi-scale roughness surface**. (A) A schematic illustration of the OCP detection set up. (B) Selectivity test using Hb MI biosensor imprinted on smooth surface to detect Hb and Mb. (C) Schematic representation of the fitting principle of small and large analytes into imprints on multi-scale roughness surface. A good fit occurs only when the analyte dimension matches the gold surface roughness.

When analyte is re-introduced, a potentiometric response occurs, or an open circuit potential (OCP) variation is established when the analyte fits accurately back into the imprinted cavity. A typical OCP vs

View Article Online
DOI: 10.1039/C6AN01157H



concentration curve for hemoglobin (Hb) is shown in Figure 3 (B). In Figure 3 (B) we show the OCP for a gold electrode imprinted for Hb and where Hb or Myoglobin (Mb) are added as the analytes. Typical OCP response curve corresponding to Hb has two domains, a linear and a plateau regime. In the linear regime the imprinted spaces are rapidly being filled up with each droplet of analyte, and hence the OCP response is linear in Hb concentration. (The OCP response can also be plotted as a function of time, as shown in figure S1, where the response time of each point is approximately 5 minutes). The biosensor is then calibrated and quantitative readouts of the Hb concentration in the analyte solution were obtained. The onset of the plateau region indicates when the imprinted cavities are completely filled and additional analytes no linger trigger an OCP. Concentrations in this regime can only elicit a yes/no response. Addition of Mb analyte does not engender an OCP response since the Mb molecule does not fit into the cavities produced by Hb. The lack of response for the analyte that does not match the imprint is an indication of high specificity of the detection method.

Another situation where a poor response can occur is when the size of the analyte is mismatched to the size of the niche in which it is imprinted, as illustrated in Figure 3(C). In this case when a small analyte is imprinted on a gold surface where the roughness was much bigger than the size of the analyte. The cavity is too big to be spanned by the imprinting thiols, as shown in the figure. On the other hand the cavities on the smoother surface are tight enough where selective adsorption of the thiols around the molecule can fill all space. The inverse situation is illustrated in bottom layer of Figure 3(C), where we have a large analyte. In this case the imprinting must be done on the rougher surface to accommodate the analyte.

### 3.4 Detection of hemoglobin under different pH

Hb is a tetramer composed of two sets of α and β subunits. It is the smallest analyst in our study, therefore, it turns out to be the best analyte to investigate how subtle conformational change can MI biosensor differentiate. The major function of Hb is to carry oxygen, which is adsorbed in the heme. The degree of oxygenation of the molecule is a function of pH where the molecule has a resonant vibration after binding.[65-67] Therefore, the structure of Hb can change significantly with different pH in aqueous solution. In order to determine if the technique is sufficiently sensitive to detect changes in morphology alone, a pH cross test was designed to investigate the limit of biosensor. For the first group, Hb was imprinted at pH 6.5 and then detected at pH ranging from 5.0 to 8.0. For the second group, Hb was imprinted at pH 5.5 and detected at pH ranging from 4.5 to 7.0. The OCP response function for each trial is plotted in Figure 4 (B) Inset. The maximum OCP response is obtained when the imprint and detection are performed at the same pH value. The Maximum OCP as a function of pH was also plotted in Figure 4 (B) and 4 (C). The maximum OCP values are similar for the electrode imprinted at 6.5 and at 5.5, indicating that the quality of SAM is not degraded in this pH range. In each case, the OCP has a normal distribution around the maximum value, indicating that the imprinting process can detect the subtle variation in the molecular structure. Based on the pH cross test, we proved that the sensor detects not only chemical differences, but

View Article Online
DOI: 10.1039/C6AN01157H



also purely molecular structure differences in the molecule. This kind of physical geometry variation is impossible to be detected through regular chemical analysis methods. Hence, the pH cross test of Hb biosensor proves the sensitivity of MI biosensor to subtle conformational change between protein molecules, such as protein misfolding.

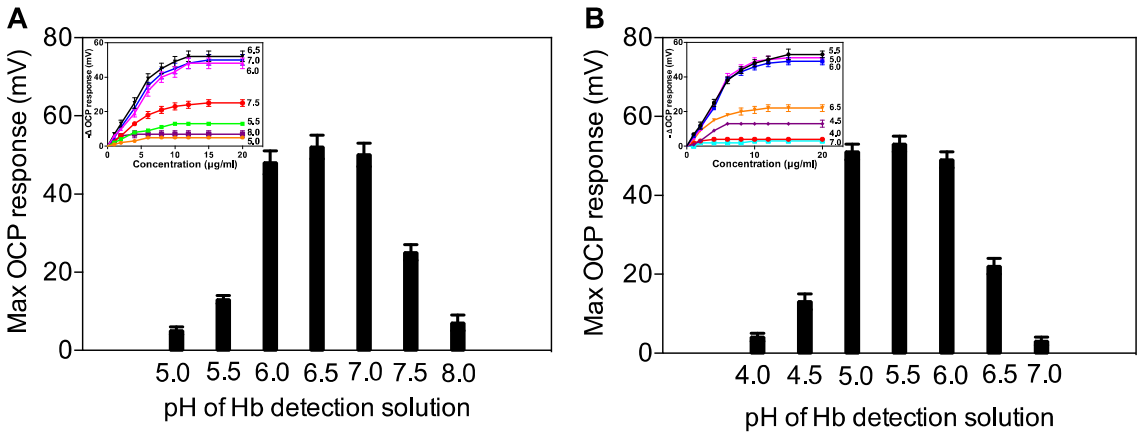


**Fig.4. pH cross test of Hb biosensor on smooth gold surface.** Hb biosensor was imprinted at A) pH = 6.5 and detected at pH 5.0 to 8.0 as well as at B) pH =5.5 and detected at pH 4.0 to 7.0. Hb is known to change its conformation and size to subtle alteration of pH values. Two Hb biosensors at either pH=6.5 or pH=5.5 were prepared. The maximum OCP response of Hb to each biosensor was studied.

### 3.5 Detection of molecular clusters: Fibrinogen and fibrin/fibrinogen complex

Fibrinogen (Fb) is a critical protein in hemostasis blood. Its structure consists of two identical halves, each formed by three non-identical poly-peptide chains, Aα, Bβ and ϒ[68, 69]. The amino termini of all six chains are disulfide-linked, forming its central or E region while disulfide-linked carboxyl terminal portions of Bβ and ϒ chains and a portion of the Aα chain form its two outer or D regions. In the inactive state fibrinogen is hydrophilic and remains in the blood steam. Fb can be activated by thrombin to induce clotting by cleaving fibrinopeptides A and B. The resulting fibrin monomer self-assembles to form fibrils which progress to fiber formation by lateral contact with one another.

Many mutations of Fb have been reported that inhibit fibrin polymerization. Currently, it is common practice to test the clotting ability of a patient's blood prior to any medical interventions. Failure to clot can have many different underlying reasons and a precise determination of the cause can be very helpful in deciding how to proceed. For example, a minor fraction of circulating Fb is clottable catabolic lacking varying parts of the C terminal region of their Aalpha chains, currently termed des-alphaC fibrinogen. Maximum OCP response is compared in Figure 5 (A) around 60 mV OCP response was obtained on the smooth surface, while almost no OCP response can be observed on rough surface. Therefore, smooth gold surface was selected for Fb imprinting. In Figure 5 (B), we imprinted Fb on smooth gold surface, and cross test with normal Fb and Des αC Fb. The cartoon in the inset shows the structure of

View Article Online
DOI: 10.1039/C6AN01157H



the fibrinogen, clearly, Des-αC fibrinogen molecule lose a part of Alpha chain. No obvious OCP response is observed when cross test with Des αC Fb, shows the great capacity of Fb biosensor to differentiate this mutated fibrinogen.

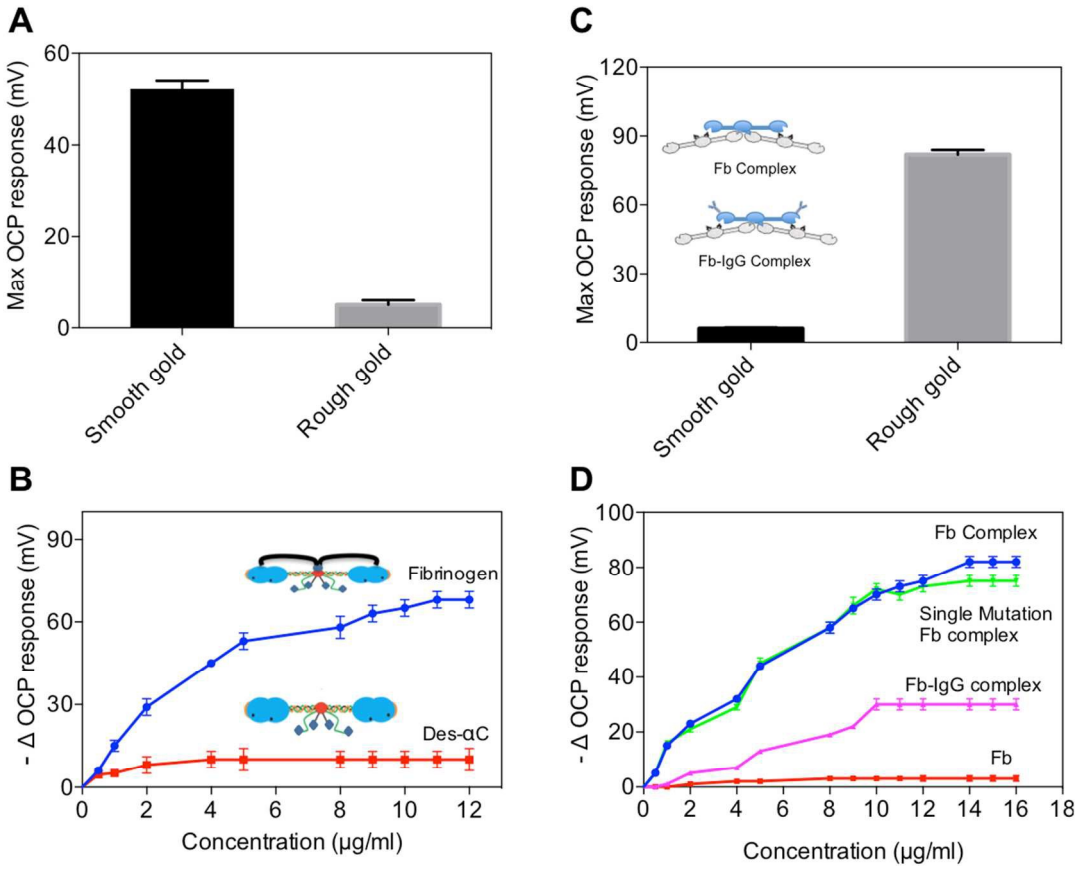


**Fig.5. Detection of Fb and Fb complex in different size scales with various MI biosensors.** (A) Maximum OCP response of Fb in small size to Fb biosensor imprinted on either smooth or rough surfaces and (B) further selectivity test of Fb MI biosensor imprinted on smooth surface to detect Fb. Des-αC Fb with same size of Fb was chosen as a control, but showed little response. Structures of normal Fb and Des-αC Fb were shown in the insets, indicating the similar size of both analytes, but with subtle difference in conformation. (C) Maximum OCP responses of Fb complex in large size to Fb complex biosensor imprinted on either smooth or rough surfaces and (D) further selectivity test of Fb complex biosensor imprinted on rough surface to detect Fb complex, Fb complex with single amino acid mutation, Fb-IgG complex and Fb respectively. Structures of Fb-IgG complex and Fb complex were shown in the insets of (C). Fb complex refers to a cluster of 3 Fb molecules. Fb complex with single amino acid mutation was unable to be differentiated, indicating the detection limit of MI biosensor.

View Article Online
DOI: 10.1039/C6AN01157H



Then we continue to study more fibrinogen type with mutation. Soluble fibrin exists in blood in complex with three fibrinogen molecules but the exact composition or complex size is not known. This complex can be measured by clinical laboratory methods, but they are not currently used since soluble fibrin is limited clinical relevance. In Figure 5 (C), maximum OCP is compared for fibrinogen complex imprinted on smooth and rough side of gold surface. No OCP response is observed on smooth gold, since the fibrinogen complex is much larger than fibrinogen molecule. Therefore, the best MI effect can be obtained on rough gold surface for fibrinogen complex.

In Figure 5 (D), the specificity of Fb complex was evaluated. Different analytes were tested with Fb complex biosensor. Another mutant of fibrinogen complex, fibrinogen-IgG complex, was cross-tested with fibrinogen complex biosensor. Around 20 mV OCP response was obtained. This OCP response probably comes from some regular fibrinogen complex still existing in the sample. Regular fibrinogen was also tested, and no OCP response was observed. In order to test the limit of the fibrinogen complex biosensor, fibrinogen complex with a single amino acid mutation was tested, and similar OCP response was generated during the detection process, which indicates the geometry of single mutation fibrinogen complex is very close to regular fibrinogen complex, and the biosensor cannot differentiate this subtle structure difference.

### 3.6 **Imprinting with viral and bacterial particles**

Detection of viral particles is commonly done via either RT-PCR or sequencing of the viral RNA or DNA. Both techniques require amplification and hence cannot be done at bedside. Our method detects the entire virion, at a sensitivity level of better than $10^6$ particles per ml. Here we tested the detection method for two viruses, polio and adenovirus. As can be seen from Figure 2(A), the poliovirus is much smaller than the Adenovirus, i.e., 30 nm vs 90 nm. The potentiometric responses for an electrode imprinted for poliovirus and cross-tested with poliovirus, on both the rough and smooth sides are shown in Figure 6(A). The sensitivity and the OCP response are both higher on the smooth surface, even though an adequate response is also obtained on the rough surface. In this case the size of the virions, approximately 30 nm, can be fit in the region of overlap between the roughness distributions of both smooth and rough surfaces.

The OCP responses for electrodes imprinted with the adenovirus, on smooth and rough surfaces are shown in Fig 6 (B) inset. This virus of much larger size, 90nm, does not produce a significant signal on the smooth surface, while a large OCP response is observed on the rough surface. The larger size of the adenovirus, 90 nm, is close to the mean value of the rough surface, and at least 3 times larger than the mean of the smooth surface. Cross testing the electrode imprinted with adenovirus with the polio virus, as shown in Fig 6 (B), does not elicit an OCP response, indicative of the ability of the sensor to differentiate between these two viruses.

View Article Online
DOI: 10.1039/C6AN01157H



Given the enhanced sensitivity we observed for larger analytes detected on imprinted rough gold surfaces, we tried to determine if the detection capacity could further be extended to bacteria. Two types of bacteria, S.Aureus and E.Coli, one gram positive with radius of 600nm and the other gram negative, with a radius of 2 µm, were tested. The OCP response as a function of concentration is shown in Figure 6 (C), for an electrode imprinted with S.Aureus and tested with both S.Aureus and E coli. A robust OCP signal is observed in both cases, indicating that, despite the large response, the MI biosensor no longer has

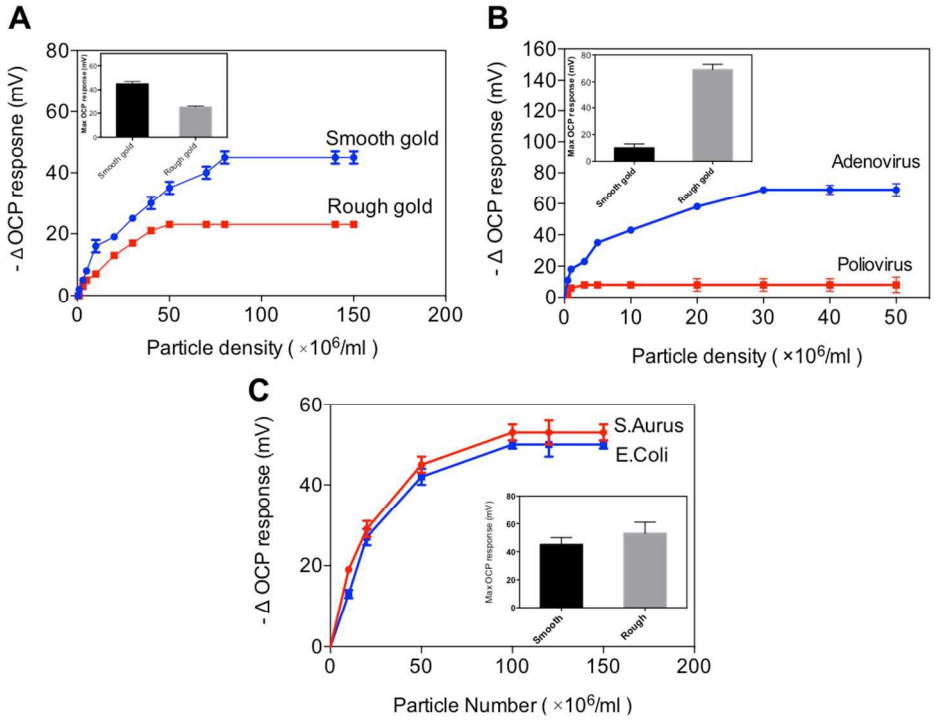


**Fig. 6. Detection of virus and bacteria with MI biosensor. (A)** OCP responses of poliovirus to poliovirus biosensor imprinted on smooth and rough gold surface. Comparison of maximum OCP response of poliovirus to poliovirus biosensor imprinted on smooth and rough gold surfaces respectively was shown in insets. **(B)** Selectivity test using adenovirus MI biosensor imprinted on smooth and rough gold surface to detect adenovirus and poliovirus. Comparison of maximum OCP response of adenovirus to adenovirus imprinted on smooth and rough gold surfaces. **(C)** Selectivity test using S. Aureus biosensor imprinted on smooth and rough gold surfaces to detect S.Aureus and E.Coli. Comparison of maximum OCP response of S.Aureus to S.Aureus biosensor imprinted on smooth and rough gold surfaces was also shown in insets. It is shown that the bacteria biosensor lost its specificity since the large size of the analyte.

specificity for bacteria. In this case, the diameters of both particles are much larger than the mean roughness of the rough gold surface, and hence can not make imprints with sufficient sensitivity to the shape of the bacteria. If we overlay the two types of bacteria on the drawing of the rough gold surface, the niche created covers less than 25% of the area of both types of bacteria. Hence even though these two

View Article Online
DOI: 10.1039/C6AN01157H



bacteria have very different structures, the imprinted area does not provide a sufficiently large area to positively identify the analyte. The OCP response obtained with bacteria is non-specific to either type of bacteria or the roughness provided by either the smooth or the rough gold surfaces. Electrodes with larger roughness possibly produced via micolithographic methods are currently being attempted.

**Discussion**

Those results taken together imply that the process through which proteins or viruses are templated, is not a two dimensional function only of the height of the SAM, as was initially postulated by Zhou[50]. Rather, the template is three-dimensional, as shown in Figures 3(C). The analyte is enveloped within the niches on the gold surface created by the substrate roughness. The SAM then forms around the analyte as it fills in and coats the wall of the niche surrounding the analyte. When the analyte is washed off, it leaves behind a three dimensional imprinted cavity complimentary with imprinted molecule, which is highly specific to the conformation of the analyte. In this case the size of the niche has to be commensurate with the dimensions of the analyte. If the niche is too large, i.e. the surface roughness is too large and the SAM layer, which is attached to the surfaces of the wall surrounding the analyte, does not come in contact with the imprinting molecule and hence fails to form an identifying pattern. Similarly, if the analyte is much larger than the niche dimensions, then only a small fraction of its surface is imprinted, and the template is not specific enough to the analyte. On the scale of Figure 2(A) we also mark with arrows the measured roughness of the smooth and rough sides of the electrode, as well as the range of roughness available on the respective surfaces. A broad spectrum of roughness is available on each surface allows for the imprinting of analytes for which the precise dimensions are not known. In fact the small region of overlap explains the ability to detect some of the molecules, such as the poliovirus on either of the two substrates. The OCP though is larger on the rough surface due to the increased surface area available for the imprint.

In Figure 2 (A) there is a critical dimension exists which separates the analytes that are best detected by the rough surface from those that are best detected on the smooth surface. Hence these results indicate that future improvements to the biosensor and in particular its ability to detect bacteria may be achieved via lithographic methods, where the roughness is exactly tailored to the analyte.

**Conclusion**

In conclusion we have shown that MI biosensors platform can be applied to a broad scale of biological molecules, such as proteins, viruses, and bacteria, ranging in size from several nanometers to hundreds of nanometers. In the case of 2D imprinting, the height of the SAM, 1.2 nm, dictated the maximum dimensions of the imprinted molecule. Here we present a model for 3D imprinting, where the analyte is sequestered within a niche within the surface roughness. The SAM is then assembled on the walls of the niche, forming a three dimensional pattern of the analyte. This then imposes the boundary conditions upon the surface morphology, where the walls must be sufficiently close to the molecule such that the SAM can form around it and mold to its contour. When this condition is satisfied, the MI method is very sensitive

View Article Online
DOI: 10.1039/C6AN01157H



and was shown to differentiate between different conformations of a molecule due to changes in pH, structural variations in proteins and positively identify viruses in liquids containing as little as $10^6$ particles.

**Reference**

1. Q. Zhang, A. Prabhu, A. San, J. F. Al-Sharab and K. Levon, *Biosens Bioelectron*, 2015, **72**, 100-106.
2. J. H. Chen, Y. L. Zhou, D. H. Wang, F. He, V. M. Rotello, K. R. Carter, J. J. Watkins and S. R. Nugen, *Lab Chip*, 2015, **15**, 3086-3094.
3. S. K. Vashist, P. B. Luppa, L. Y. Yeo, A. Ozcan and J. H. Luong, *Trends Biotechnol*, 2015, **33**, 692-705.
4. J. Wang, *Biosens Bioelectron*, 2006, **21**, 1887-1892.
5. G. J. Kost, *Kost GJ (ed)*, 2002, 3-12.
6. J. Wang, *Nucleic Acids Research*, 2000, **28**, 3011-3016.
7. T. Laksanasopin, T. W. Guo, S. Nayak, A. A. Sridhara, S. Xie, O. O. Olowookere, P. Cadinu, F. Meng, N. H. Chee, J. Kim, C. D. Chin, E. Munyazesa, P. Mugwaneza, A. J. Rai, V. Mugisha, A. R. Castro, D. Steinmiller, V. Linder, J. E. Justman, S. Nsanzimana and S. K. Sia, *Sci Transl Med*, 2015, **7**, 273re271.
8. Q. Zhang, H. S. Majumdar, M. Kaisti, A. Prabhu, A. Ivaska, R. Osterbacka, A. Rahman and K. Levon, *Ieee T Electron Dev*, 2015, **62**, 1291-1298.
9. T. Zhou, Y. Feng, L. Zhou, Y. Tao, D. Luo, T. Jing, X. Shen, Y. Zhou and S. Mei, *Sensors and Actuators B: Chemical*, 2016, **236**, 153-162.
10. M. L. Yola, V. K. Gupta and N. Atar, *Mat Sci Eng C-Mater*, 2016, **61**, 368-375.
11. N. Atar, M. L. Yola and T. Eren, *Applied Surface Science*, 2016, **362**, 315-322.
12. C. d. S. Moreira, L. C. Oliveira, R. Fischer, E. S. Medeiros, A. M. N. Lima and H. Neff, *Research on Biomedical Engineering*, 2016, 0-0.
13. J. M. Rothberg, W. Hinz, T. M. Rearick, J. Schultz, W. Mileski, M. Davey, J. H. Leamon, K. Johnson, M. J. Milgrew and M. Edwards, *Nature*, 2011, **475**, 348-352.
14. H. H. Xiao, H. Q. Song, Y. Zhang, R. G. Qi, R. Wang, Z. G. Xie, Y. B. Huang, Y. X. Li, Y. Wu and X. B. Jing, *Biomaterials*, 2012, **33**, 8657-8669.
15. H. H. Xiao, R. G. Qi, S. Liu, X. L. Hu, T. C. Duan, Y. H. Zheng, Y. B. Huang and X. B. Jing, *Biomaterials*, 2011, **32**, 7732-7739.
16. H. H. Xiao, W. L. Li, R. G. Qi, L. S. Yan, R. Wang, S. Liu, Y. H. Zheng, Z. G. Xie, Y. B. Huang and X. B. Jing, *J Control Release*, 2012, **163**, 304-314.
17. H. H. Xiao, H. Q. Song, Q. Yang, H. D. Cai, R. G. Qi, L. S. Yan, S. Liu, Y. H. Zheng, Y. B. Huang, T. J. Liu and X. B. Jing, *Biomaterials*, 2012, **33**, 6507-6519.
18. H. H. Xiao, G. T. Noble, J. F. Stefanick, R. G. Qi, T. Kiziltepe, X. B. Jing and B. Bilgicer, *J Control Release*, 2014, **173**, 11-17.
19. J. T. Dias, L. Lama, J. Gantelius and H. Andersson-Svahn, *Nanoscale*, 2016, **8**, 8195-8201.
20. A. W. Holle, X. Y. Tang, D. Vijayraghavan, L. G. Vincent, A. Fuhrmann, Y. S. Choi, J. C. del Alamo and A. J. Engler, *Stem Cells*, 2013, **31**, 2467-2477.
21. P. A. He, Y. Xu and Y. Z. Fang, *Anal Lett*, 2005, **38**, 2597-2623.

View Article Online
DOI: 10.1039/C6AN01157H



22. G. A. Rivas, M. L. Pedano and N. F. Ferreyra, *Anal Lett*, 2005, **38**, 2653-2703.
23. P. Miao, Y. Tang and J. Yin, *Chem Commun (Camb)*, 2015, **51**, 15629-15632.
24. P. Miao, Y. G. Tang, B. D. Wang, C. M. Jiang, L. Q. Gao, B. Bo and J. Wang, *Electrochim Acta*, 2016, **190**, 396-401.
25. P. Miao, B. Wang, Z. Yu, J. Zhao and Y. Tang, *Biosens Bioelectron*, 2015, **63**, 365-370.
26. J. H. Chen, Z. W. Jiang, J. D. Ackerman, M. Yazdani, S. Hou, S. R. Nugen and V. M. Rotello, *Analyst*, 2015, **140**, 4991-4996.
27. J. H. Chen, B. Duncan, Z. Y. Wang, L. S. Wang, V. M. Rotello and S. R. Nugen, *Nanoscale*, 2015, **7**, 16230-16236.
28. Y. X. Huang, X. C. Dong, Y. M. Shi, C. M. Li, L. J. Li and P. Chen, *Nanoscale*, 2010, **2**, 1485-1488.
29. J. R. Choi, J. Hu, R. H. Tang, Y. Gong, S. S. Feng, H. Ren, T. Wen, X. J. Li, W. A. W. Abas, B. Pingguan-Murphy and F. Xu, *Lab Chip*, 2016, **16**, 611-621.
30. B. Rizal, M. M. Archibald, T. Connolly, S. Shepard, M. J. Burns, T. C. Chiles and M. J. Naughton, *Analytical chemistry*, 2013, **85**, 10040-10044.
31. M. Cohen-Atiya and D. Mandler, *J Electroanal Chem*, 2003, **550**, 267-276.
32. A. Duzgun, H. Imran, K. Levon and F. X. Rius, *Sci World J*, 2013, DOI: Artn 282756
Doi 10.1155/2013/282756.
33. Y. Zhou, B. Yu, A. Guiseppi-Elie, V. Sergeyev and K. Levon, *Biosens Bioelectron*, 2009, **24**, 3275-3280.
34. Y. T. Wang, M. Rafailovich, Z. Q. Zhang, B. Rigas, K. Levon, S. Mueller, V. Jain, J. J. Yi and J. Sokolov, *Abstr Pap Am Chem S*, 2007, **234**.
35. M. Monier, D. A. Abdel-Latif and Y. G. Abou El-Reash, *Journal of colloid and interface science*, 2016, **469**, 344-354.
36. M. H. Abdalhai, A. n. M. Fernandes, X. Xia, A. Musa, J. Ji and X. Sun, *Journal of agricultural and food chemistry*, 2015, **63**, 5017-5025.
37. M. L. Yola, T. Eren and N. Atar, *Biosens Bioelectron*, 2014, **60**, 277-285.
38. V. K. Gupta, M. L. Yola, T. Eren and N. Atar, *Sensors and Actuators B: Chemical*, 2015, **218**, 215-221.
39. A. J. Kell, L. Page, S. Tan, I. Charlebois, M. Boissinot, M. LeClerc and B. Simard, *Nanoscale*, 2011, **3**, 3747-3754.
40. Z. Dai, X. Hu, H. Wu and X. Y. Zou, *Chem Commun*, 2012, **48**, 1769-1771.
41. J. Chen, A. A. Jackson, V. M. Rotello and S. R. Nugen, *Small*, 2016, DOI: 10.1002/smll.201503682.
42. B. Ertan, T. Eren, İ. Ermiş, H. Saral, N. Atar and M. L. Yola, *Journal of colloid and interface science*, 2016, **470**, 14-21.
43. L. D. Bolisay, J. N. Culver and P. Kofinas, *Biomaterials*, 2006, **27**, 4165-4168.
44. K. Flavin and M. Resmini, *Anal Bioanal Chem*, 2009, **393**, 437-444.
45. D. Kriz, O. Ramström and K. Mosbach, *Analytical chemistry*, 1997, **69**, 345A-349A.
46. Y. T. Wang, Z. Q. Zhang, V. Jain, J. J. Yi, S. Mueller, J. Sokolov, Z. X. Liu, K. Levon, B. Rigas and M. H. Rafailovich, *Sensor Actuat B-Chem*, 2010, **146**, 381-387.
47. K. Fukazawa, Q. Li, S. Seeger and K. Ishihara, *Biosens Bioelectron*, 2013, **40**, 96-101.

View Article Online
DOI: 10.1039/C6AN01157H



48. N. Atar, T. Eren, M. L. Yola and S. B. Wang, *Sensor Actuat B-Chem*, 2015, **216**, 638-644.
49. V. K. Gupta, M. L. Yola and N. Atar, *Sensor Actuat B-Chem*, 2014, **194**, 79-85.
50. Y. X. Zhou, B. Yu and K. Levon, *Chem Mater*, 2003, **15**, 2774-2779.
51. Y. T. Wang, Y. X. Zhou, J. Sokolov, B. Rigas, K. Levon and M. Rafailovich, *Biosens Bioelectron*, 2008, **24**, 162-166.
52. Y. X. Zhou, B. Yu and K. Levon, *Abstr Pap Am Chem S*, 2003, **225**, U128-U128.
53. Y. Yu, Q. Zhang, J. Buscaglia, Y. Wang, C.-C. Chang, Y. Liu, Y. Guo, Z. Yang, K. Levon and M. H. Rafailovich, *Analyst*, 2016.
54. M. W. Mosesson, N. Alkjaersig, B. Sweet and S. Sherry, *Biochemistry*, 1967, **6**, 3279-3287.
55. M. W. Mosesson and S. Sherry, *Biochemistry*, 1966, **5**, 2829-&.
56. D. Galanakis, M. Refailovich, L. Zhang, B. Casey and V. K., *J Thromb Hemost* 2015;, **13**, 581.
57. C. Vericat, M. Vela, G. Benitez, P. Carro and R. Salvarezza, *Chemical Society Reviews*, 2010, **39**, 1805-1834.
58. H. P. Erickson, *Biol Proced Online*, 2009, **11**, 32-51.
59. G. A. Ordway and D. J. Garry, *J Exp Biol*, 2004, **207**, 3441-3446.
60. M. K. Boehm, M. O. Mayans, J. D. Thornton, R. H. J. Begent, P. A. Keep and S. J. Perkins, *J Mol Biol*, 1996, **259**, 718-736.
61. J. Cello, A. V. Paul and E. Wimmer, *Science*, 2002, **297**, 1016-1018.
62. D. J. Spector, *Virology*, 2007, **359**, 116-125.
63. J. Kluytmans, A. vanBelkum and H. Verbrugh, *Clin Microbiol Rev*, 1997, **10**, 505-&.
64. G. Reshes, S. Vanounou, I. Fishov and M. Feingold, *Biophys J*, 2008, **94**, 251-264.
65. M. Mahato, P. Pal, T. Kamilya, R. Sarkar and G. B. Talapatra, *J Phys Chem B*, 2010, **114**, 495-502.
66. F. Hook, M. Rodahl, B. Kasemo and P. Brzezinski, *P Natl Acad Sci USA*, 1998, **95**, 12271-12276.
67. E. N. Samuelsen, A. K. Imsland and O. Brix, *Fish Physiol Biochem*, 1999, **20**, 135-141.
68. J. Koo, D. Galanakis, Y. Liu, A. Ramek, A. Fields, X. Ba, M. Simon and M. H. Rafailovich, *Biomacromolecules*, 2012, **13**, 1259-1268.
69. J. Koo, M. H. Rafailovich, L. Medved, G. Tsurupa, B. J. Kudryk, Y. Liu and D. K. Galanakis, *Journal of thrombosis and haemostasis : JTH*, 2010, **8**, 2727-2735.

View Article Online
DOI: 10.1039/C6AN01157H



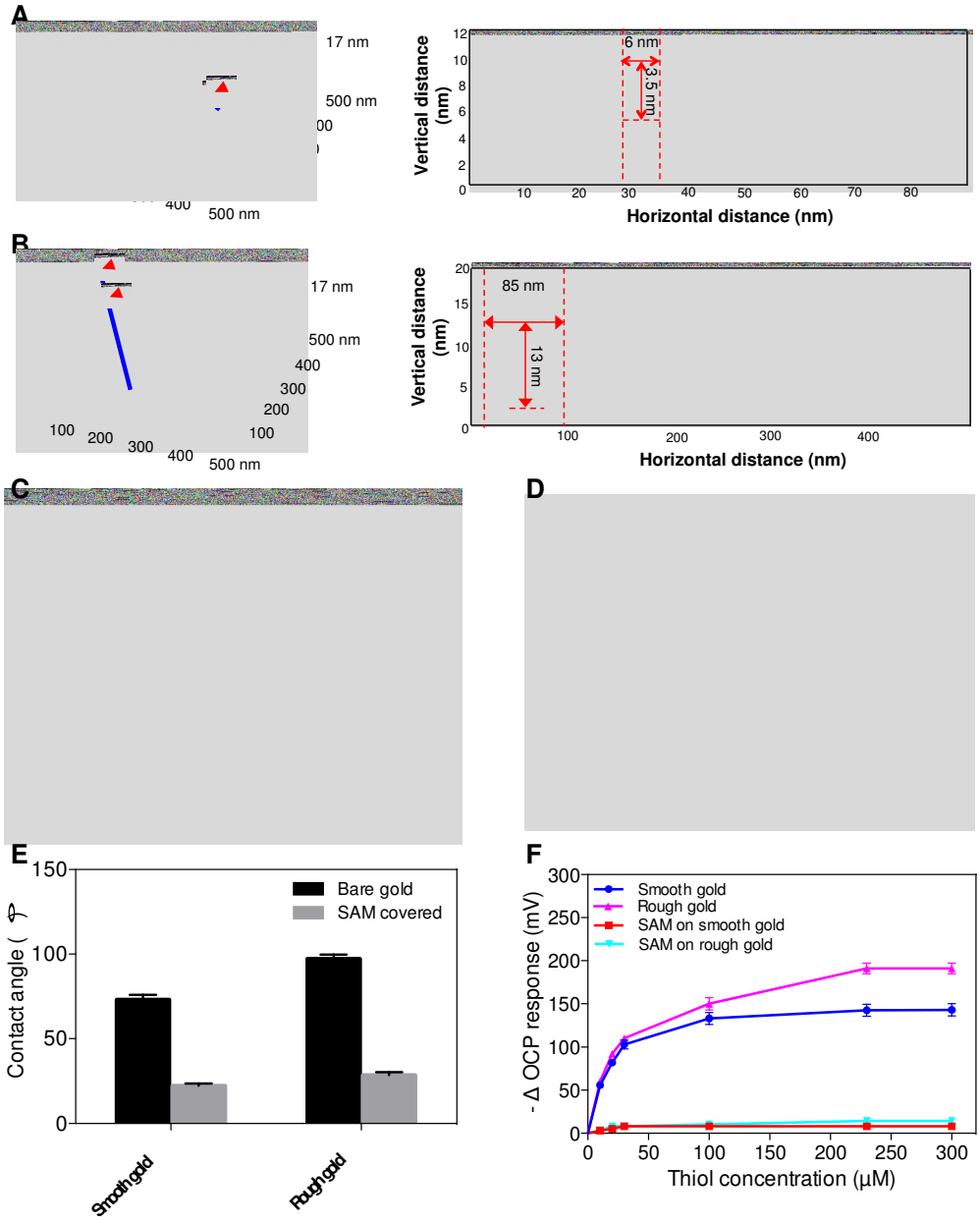


**Fig.1. Surface characterization of multi-scale roughness gold surfaces.** AFM topographical scan and the associated cross sectional analysis for A) smooth and B) rough gold surfaces. Further description of the surfaces by histogram of C) horizontal and D) vertical surface roughness for smooth and rough gold surfaces is shown. Comparison between smooth and rough surfaces before (bare gold) and after (SAM covered) SAM formation characterized by E) contact angle and F) potentiometric titration with thiol solution. Similar chemistry property was found on both smooth and rough gold surfaces after SAM formation, despite of the large physical roughness difference between them.

View Article Online
DOI: 10.1039/C6AN01157H



Table 1 Summary of the sizes and molecular weights of analytes in this study

| Analyte | $M_w(\times 10^3)$ | Dimension (nm) | Shape | Reference |
|---|---|---|---|---|
| Mb | 17.6 | 3.5×2×4.5 | Rectangle | 40 |
| Hb | 64.5 | 5×5×5 | Rectangle | 41 |
| CEA | 200 | 8×28† | Cylinder | 42 |
| Fb | 340 | 9×6×47 | Rectangle | 40 |
| Poliovirus | N/A | 20 ‡ | Sphere | 43 |
| Adenovirus | N/A | 90 ‡ | Sphere | 44 |
| S. Aureus | N/A | 600 ‡ | Sphere | 45 |
| E.Coli | N/A | 500×2000† | Cylinder | 46 |

† The shape of molecule is cylinder, the first number represents the radius of undersurface, and the second number represents the height of cylinder.

‡ The shape of the molecules is sphere; the number represents the diameter of the sphere.

View Article Online
DOI: 10.1039/C6AN01157H



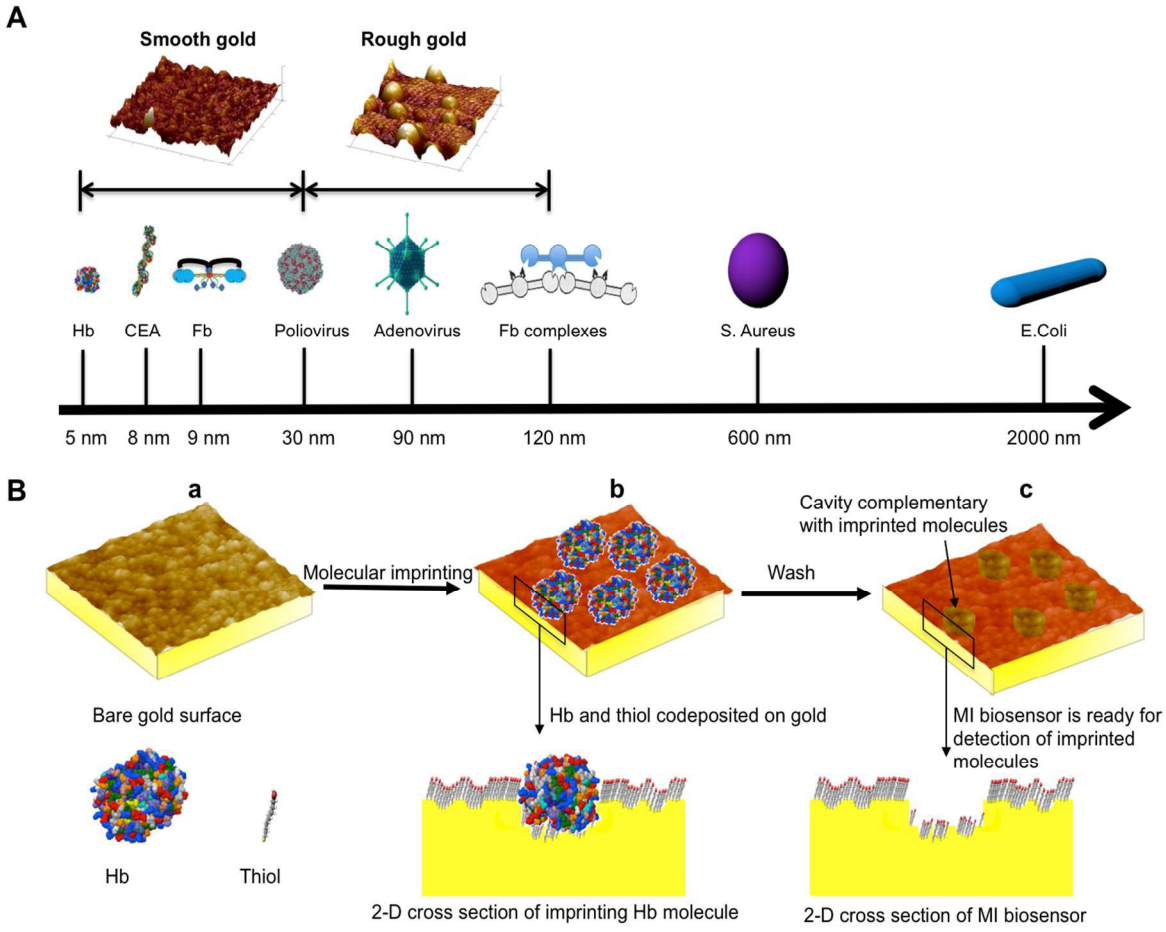


**Fig.2. A summary of possible analytes and fabrication process of the MI biosensor .** (A) Size distribution of the possible analytes in this study, including protein, antigen, virus and bacteria in different sizes, as plotted on a nanometer scale chart. (B) Schematic illustration and cross-sectional of the 3D MI biosensor fabrication process. The red-color layer represents SAM coverage.

View Article Online
DOI: 10.1039/C6AN01157H



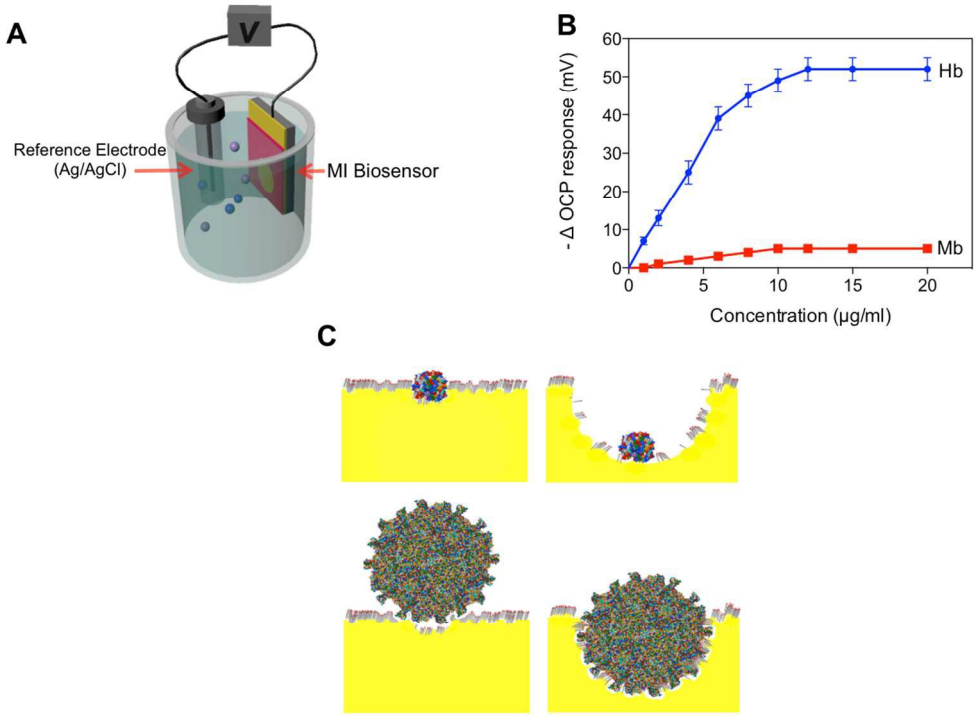


**Fig.3. OCP detection method on multi-scale roughness surface**. (A) A schematic illustration of the OCP detection set up. (B) Selectivity test using Hb MI biosensor imprinted on smooth surface to detect Hb and Mb. (C) Schematic representation of the fitting principle of small and large analytes into imprints on multi-scale roughness surface. A good fit occurs only when the analyte dimension matches the gold surface roughness.

View Article Online
DOI: 10.1039/C6AN01157H



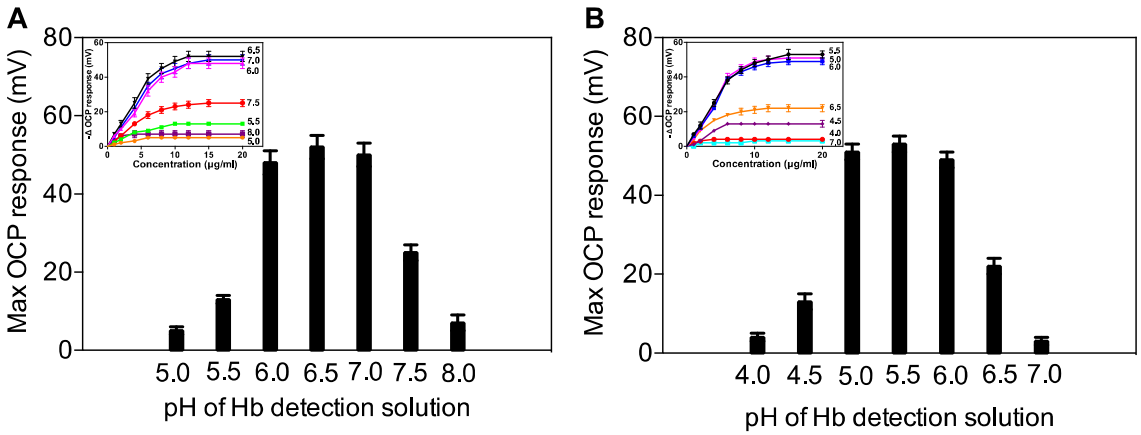


**Fig.4. pH cross test of Hb biosensor on smooth gold surface.** Hb biosensor was imprinted at A) pH = 6.5 and detected at pH 5.0 to 8.0 as well as at B) pH =5.5 and detected at pH 4.0 to 7.0. Hb is known to change its conformation and size to subtle alteration of pH values. Two Hb biosensors at either pH=6.5 or pH=5.5 were prepared. The maximum OCP response of Hb to each biosensor was studied.

View Article Online
DOI: 10.1039/C6AN01157H



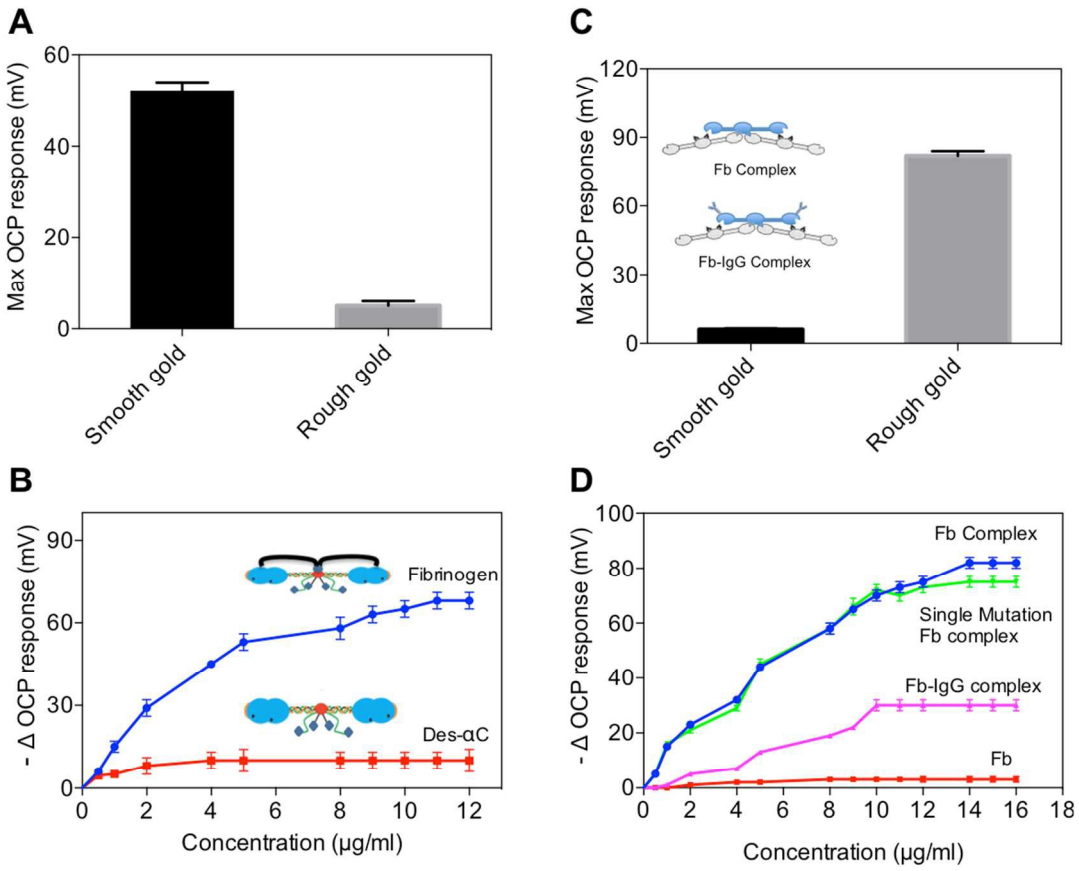


**Fig.5. Detection of Fb and Fb complex in different size scales with various MI biosensors.** (A) Maximum OCP response of Fb in small size to Fb biosensor imprinted on either smooth or rough surfaces and (B) further selectivity test of Fb MI biosensor imprinted on smooth surface to detect Fb. Des-αC Fb with same size of Fb was chosen as a control, but showed little response. Structures of normal Fb and Des-αC Fb were shown in the insets, indicating the similar size of both analytes, but with subtle difference in conformation. (C) Maximum OCP responses of Fb complex in large size to Fb complex biosensor imprinted on either smooth or rough surfaces and (D) further selectivity test of Fb complex biosensor imprinted on rough surface to detect Fb complex, Fb complex with single amino acid mutation, Fb-IgG complex and Fb respectively. Structures of Fb-IgG complex and Fb complex were shown in the insets of (C). Fb complex refers to a cluster of 3 Fb molecules. Fb complex with single amino acid mutation was unable to be differentiated, indicating the detection limit of MI biosensor.

View Article Online
DOI: 10.1039/C6AN01157H

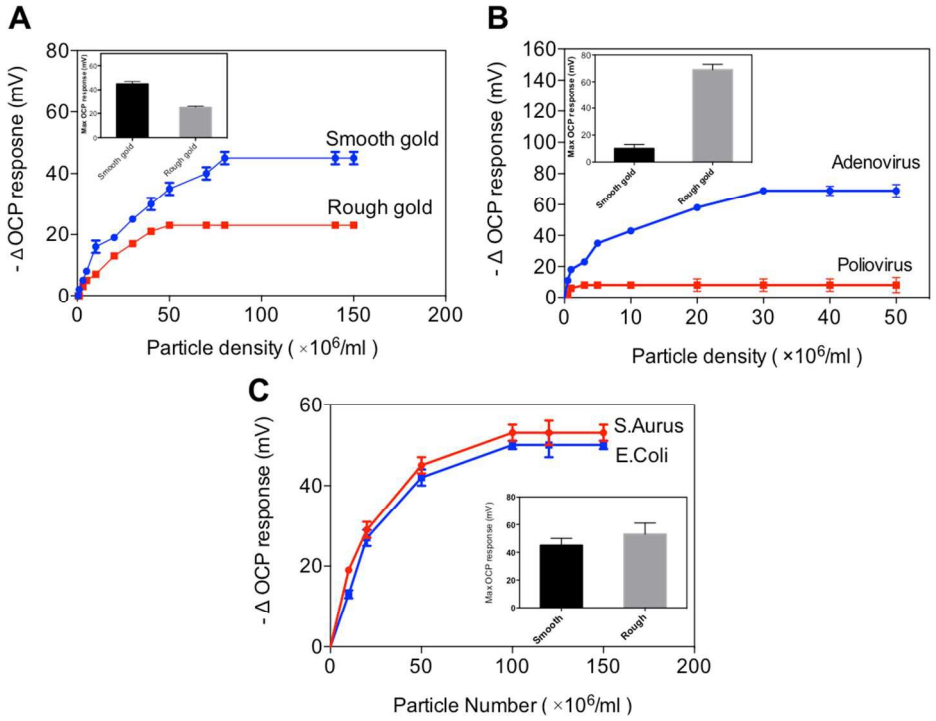


**Fig. 6. Detection of virus and bacteria with MI biosensor. (A)** OCP responses of poliovirus to poliovirus biosensor imprinted on smooth and rough gold surface. Comparison of maximum OCP response of poliovirus to poliovirus biosensor imprinted on smooth and rough gold surfaces respectively was shown in insets. **(B)** Selectivity test using adenovirus MI biosensor imprinted on smooth and rough gold surface to detect adenovirus and poliovirus. Comparison of maximum OCP response of adenovirus to adenovirus imprinted on smooth and rough gold surfaces. **(C)** Selectivity test using S. Aureus biosensor imprinted on smooth and rough gold surfaces to detect S.Aureus and E.Coli. Comparison of maximum OCP response of S.Aureus to S.Aureus biosensor imprinted on smooth and rough gold surfaces was also shown in insets. It is shown that the bacteria biosensor lost its specificity since the large size of the analyte.